Fire Technology, 47, 985–1016, 2011

DOI: 10.1007/s10694-009-0123-7

# Compressive Response of Composites Under Combined Fire and Compression Loading

*Liu Liu, John W. Holmes and George A. Kardomateas*, Georgia Institute of Technology, Atlata, GA, USA*

*Victor Birman, Missouri University of Science and Technology, St. Louis, MO, USA*

***Abstract.*** The thermal buckling of an axially restrained composite column that is exposed to a heat flux due to fire is studied by both analytical and experimental means. The column is exposed to fire from one-side and the resulting heat damage, the charred layer formation and non-uniform transient temperature distribution are calculated by the thermal model developed by Gibson et al. (Revue de l'Institute Francais du Petrole 50:69–74, 1995). For the thermal buckling analysis, the mechanical properties of the fire-damaged (charred) region are considered negligible; the degradation of the elastic properties with temperature (especially near the glass transition temperature of the matrix) in the undamaged layer, is accounted for by using experimental data for the elastic moduli. Due to the non-uniform stiffness and the effect of the ensuing thermal moment, the structure behaves like an imperfect column, and responds by bending rather than buckling in the classical Euler (bifurcation) sense. Another important effect of the non-uniform temperature is that the neutral axis moves away from the centroid of the cross section, resulting in another moment due to eccentric loading, which would tend to bend the structure away from the fire. In order to verify the mechanical response, the compressive buckling behavior of the same material subjected to simultaneous high intensity surface heating and axial compressive loading were investigated experimentally. Fire exposure was simulated by subjecting the surface of rectangular specimens to radiant heating in a cone calorimeter. Heat flux levels of 25 kW/m$^2$, 50 kW/m$^2$ and 75 kW/m$^2$ were studied. All specimens exhibited buckling and subsequent catastrophic failure, even at compressive stresses as low as 3.5 MPa under a surface heat flux of 25 kW/m$^2$. Details of the experimental procedure, including modifications made to a cone calorimeter to allow simultaneous mechanical loading are presented.

**Keywords:** Fire, Buckling, Thermal, Composites, Column

## 1. Introduction

Fiber reinforced polymeric composites are used extensively in aerospace, marine, infrastructure and chemical processing applications. In these applications, fire

* Correspondence should be addressed to: George A. Kardomateas, E-mail: george.kardomateas@aerospace.gatech.edu

events and their resulting effects on the structural integrity are of considerable concern. In addition to the implications for design, quantitative information regarding the nature of the strength loss is required to make decisions regarding, for example, the seaworthiness of a ship that has sustained fire damage.

Many of the thermal properties of composites related to fire have been thoroughly studied and are well understood, including ignition times, heat release rates, smoke production rates and gas emissions [1–6]. Also, some recent work into the post-fire residual properties showed large reductions to the edgewise compression properties of phenolic-based sandwich composites despite having good flame resistance [6]. However, one important gap in the understanding of composites is their response and structural integrity due to the combined effect of mechanical loading and thermal loading due to fire. This paper addresses this issue, both from analysis and experiments, as far as compressive loading, which in an otherwise purely mechanical loading (no fire) would lead to bifurcational (Euler) buckling.

## 2. Theoretical Developments

### 2.1. Thermal Model for the Temperature and Char Distribution

The problem of predicting the behavior of polymer composite materials exposed to a fire environment may be divided into two parts: internal and external processes. The internal processes include all the physical and chemical processes which occur in any laminate. The external processes address, itself, first to the determination of the shape, size and intensity of the flame in the boundary layer and, second to heat transfer from this frame over the related laminate to others. The finite element model used in the paper to predict the behavior of GRP laminated in a fire environment is based on the mathematical model proposed by Henderson et al. [7] and developed by Gibson et al. [8] and Looyeh et al. [9]. The non-linear partial differential equations that govern the behavior of the laminate in the fire have been solved numerically using a mixed explicit-implicit finite element technique. Accordingly, the remaining resin material versus exposure time can be obtained. Based on the experiments and calculations performed by Gibson et al. [10], we assume that when the residual resin content is less than 80% the material can be treated as charred.

### 2.2. Thermal Buckling Analysis

The predicted temperature and charred layer thickness distribution with time along the thickness direction are obtained by the thermal finite element model discussed in the previous section. Now the quasi-static assumption is made to analyze the thermal buckling response of the column consisting of an undamaged layer and a charred layer, as shown in Figure 1. The quasi-static assumption means at each different time, the column is in an equilibrium state and the temperature distribution and the charred layer thickness at that time obtained by the finite element model can be used in the static buckling analysis. The length and total thickness of the column are denoted by $L$ and $H$, respectively. The thickness

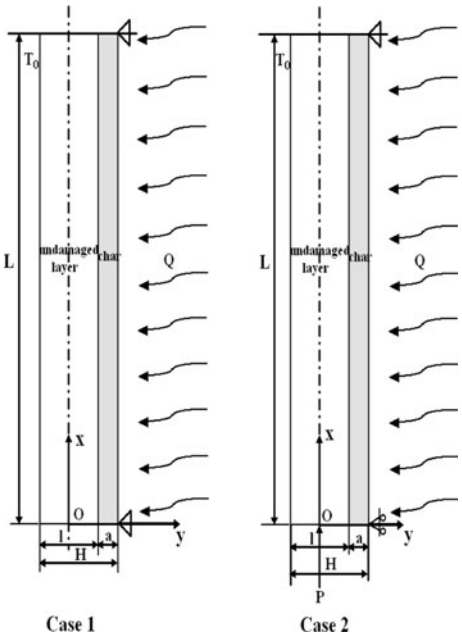


**Figure 1. Definition of the geometry for the laminated column, which is composed of an undamaged layer and a charred layer, and is subjected to a heat flux due to fire, *Q*, and a compressive load, *P*. Case 1 is a constrained column and Case 2 an unconstrained one (free to move axially).**

of the undamaged layer is represented by $l$, which is dependent on the time, $t$. It is reasonable to assume that the mechanical properties of the charred (fire-damaged) layer are negligible because of the thermal decomposition of resin material; this assumption was also made by Mouritz and Mathys [11]. Therefore, we only considered the undamaged layer in the thermal buckling analysis, and the temperature distribution in the undamaged region has been obtained (which, nevertheless, is influenced by the existence of the char layer).

Regarding the Young's modulus, $E$, of the undamaged composite, it is well known that the modulus of polymers depends strongly on the temperature and especially on how close the temperature is to the glass transition temperature, $T_g$, of the matrix. A recent paper by Kulcarni and Gibson [12] studied the effects of temperature on the elastic modulus of E-glass/vinyl ester composites. They provided measurements of temperature dependence of the elastic modulus of the composite in the range of 20°C to 140°C. The glass transition temperature of the matrix was $T_g = 130$°C. Near this temperature, the elastic modulus shows a significant variation, but below $T_g$ the variation is small. The variation of the modulus in Kulcarni and Gibson [12] fits a 3rd order polynomial equation very well (as we show later in Figure 4). If we denote the modulus, $E_0$, at room temperature, $T_0 = 20$°C, then the modulus $E$ at the temperature $T$ is a function of temperature:

$$\frac{E}{E_0} = 1 - a_1\left(\frac{T-T_0}{T_g-T_0}\right) + a_2\left(\frac{T-T_0}{T_g-T_0}\right)^2 - a_3\left(\frac{T-T_0}{T_g-T_0}\right)^3 = 1 - a_1\left(\frac{\Delta T}{\Delta T_g}\right) + a_2\left(\frac{\Delta T}{\Delta T_g}\right)^2 - a_3\left(\frac{\Delta T}{\Delta T_g}\right)^3 \quad (1)$$

For the present E-glass/vinyl ester, $E_0$ = 20.6 GPa and $a_1$ = 0.348, $a_2$ = 0.715 and $a_3$ = 0.843. The composite studied has a fiber volume fraction of 0.516 and consists of four sub-layers with the orientation of each sub-layer [0/90/+45/−45/Random]. Equation 1 captures the physics of the non-linear dependence of the composite modulus on the glass transition temperature of the matrix, $T_g$. Temperature distribution in the undamaged layer, $\Delta T$, can be determined from the finite element analysis, as described in the previous section. In order to simplify the formulations in the thermal buckling analysis, the axis $x$ is located at the mid-surface of the undamaged layer, as shown in Figure 1.

We define an "average" modulus $E_{av}$ and "a first and second moment" of the modulus with respect to the mid-surface $y$-axis, $E_{m1}$ and $E_{m2}$, respectively, by:

$$E_{av}A = \int_A E\,dA;\; E_{m1}lA = \int_A Ey\,dA;\; E_{m2}I = \int_A Ey^2\,dA, \quad (2)$$

where $A$ is the cross sectional area of the undamaged layer, $l$ is the thickness of the undamaged layer; and $I$ is the moment of inertia ($I = \int_A y^2\,dA$). The integral is evaluated numerically as the modulus $E$ is dependent on the temperature distribution, which has been solved numerically.

Due to the non-uniform modulus $E$, the neutral axis of the column is not at the mid-surface. The distance, $e$, of the neutral axis from the mid-surface axis, $x$, is determined from:

$$e\int_A E(y)dA = \int_A E(y)\,y\,dA, \quad (3)$$

which, by use of Equation 2 leads to:

$$e = E_{m1}\,l\,/E_{av}. \quad (4)$$

Assuming the longitudinal thermal expansion coefficient, $\alpha_l$, is independent of temperature, then the thermal force along the longitudinal axis, $x$, is:

$$N_x^T = \int_A E(y)\,\alpha_l\,\Delta T(y)dA, \quad (5)$$

which, by use of Equation 2 and the temperature distribution results, can be evaluated numerically.

The thermal force develops due to the constraints at both ends of the column, which causes buckling. However, the problem is not a bifurcation buckling because a thermal moment also develops. The thermal moment (with respect to the neutral axis of the column) is:

$$M_Z^T = \int_A E(y)\,\alpha_l\,\Delta T(y)\;(y-e)dA, \tag{6}$$

and this would cause bending of the column.

The problem now is to determine the response of the column under the influence of both $N_x^T$ and $M_Z^T$, which changes the character of the problem from bifurcation buckling to a bending problem. That is, the column will bend as $M_Z^T$ is applied.

We consider two cases: one is the column constrained at the two ends, which cannot move axially (Figure 1, Case 1); the other is the column under a certain constant applied load $P$, but ends free to move axially (Figure 1, Case 2). First of all, we assume the external support force $P$ that develops due to the boundaries is large enough to constrain the column, which means both ends of the column are immovable. The axial force $N_x$ does not vary with the axial position $x$. Thus, it can be seen that $N_x^T$ is equal to $-P$, due to the axial equilibrium. However, unlike the case of a uniformly heated column, the force $P$ is less than $N_x^T$ because of the thermal moment $M_x^T$. That is, the column bends away from its original straight configuration due to the thermal moment $M_x^T$, which relieves some of the external support force at the immovable ends.

Notice that $P$ is a derived quantity, not a controlled quantity at the first case of immovable ends. The controlled quantity is the thermal loading due to the fire, and the response quantity is the mid-span transverse deflection of the column.

Let us denote by $u_0$ and $w_0$ the displacements along the $x$ and $y$ directions at the neutral axis and by $\theta$ the rotation of the cross section due to bending. The non-linear strain at the neutral axis $y = e$ is:

$$\varepsilon_0 = u_{0,x} + \frac{1}{2}\theta^2. \tag{7}$$

In the following we account for the transverse shear following the procedure in Huang and Kardomateas [13]. In particular, we can set:

$$\frac{dw}{dx} = \sin\left(\theta + \gamma_{eq}\right), \tag{8}$$

where $\gamma_{eq}$ is the equivalent shear angle, i.e. the difference between the slope of the deflected column axis and the rotation $\theta$ of the cross-section due to bending.

It is reasonable to assume the shear modulus, $G$, changes with temperature in the same manner as the elastic Young's modulus, $E$. We can write:

$$\frac{G}{G_0} = 1 - a_1\left(\frac{T - T_0}{T_g - T_0}\right) + a_2\left(\frac{T - T_0}{T_g - T_0}\right)^2 - a_3\left(\frac{T - T_0}{T_g - T_0}\right)^3 = 1 - a_1\left(\frac{\Delta T}{\Delta T_g}\right) + a_2\left(\frac{\Delta T}{\Delta T_g}\right)^2 - a_3\left(\frac{\Delta T}{\Delta T_g}\right)^3. \tag{9}$$

An effective shear modulus, $\overline{G}$ is now defined based on the shear compliance as [13]:

$$\frac{l}{\overline{G}} = \int_{-l/2}^{l/2} \frac{dy}{G(y)}. \tag{10}$$

The equivalent shear angle, $\gamma_{eq}$, is defined as:

$$\gamma_{eq} = \frac{\beta P \sin\theta}{\overline{G}A}, \tag{11}$$

where $\beta$ is the shear correction factor which accounts for the non-uniform distribution of shear stresses throughout the cross section.

Then, the strain at an arbitrary point, $\overline{\varepsilon}(x, y)$, can be represented by:

$$\overline{\varepsilon} = \varepsilon_0(x) - (y - e)\frac{d(\theta + \gamma_{eq})}{dx}. \tag{12}$$

When the resulting force from Equation 12 is integrated throughout the section, the resultant should equal $-P + N_x^T$, i.e.:

$$\int_A E(y)\,\overline{\varepsilon}(x, y)dA = -P + N_x^T. \tag{13}$$

Then, by use of Equations 7 and 11, Equation 13 becomes:

$$E_{av}A\left(u_{0,x} + \frac{1}{2}\theta^2\right) + (E_{av}e - E_{m1}h)A\left(1 + \frac{\beta P\cos\theta}{\overline{G}A}\right)\theta_x = N_x^T - P \tag{14}$$

and by use of Equation 4 results in:

$$u_{0,x} = \frac{N_x^T - P}{E_{av}A} - \frac{1}{2}\theta^2, \tag{15}$$

which we can integrate over the length of the column subject to the boundary conditions that the ends are restrained in the axial direction, i.e. $u_0(0) = 0$ and $u_0(L) = 0$.

Therefore, we obtain the following:

$$\left(N_x^T - P\right)\frac{L}{E_{av}A} - \frac{1}{2}\int_0^L \theta^2\, dx = 0, \tag{16}$$

which is applicable for the entire loading range of the column and is a "constraint equation" expressing the condition that the overall change in axial displacement between the end supports must be zero because the two ends of the beam are immovable and there is a support load $P$.

Now, the bending rigidity, $(EI)_{eq}$ of the column, is likewise influenced by the non-uniform stiffness and is defined by:

$$(EI)_{eq} = \int_a E(y)\,(y-e)^2 dA. \tag{17}$$

By use of Equation 2, this results in:

$$(EI)_{eq} = E_{m2}I - \frac{E_{m1}^2 l^2 A}{E_{av}}. \tag{18}$$

Next, we modify the column equation to consider the thermal loading including thermal force and moment, and moderately large deflections. Transverse shear will also be included. In doing so, we shall properly modify the equations developed in Huang and Kardomateas [13]. The moment including the thermal effect is given by:

$$M = -(EI)_{eq}\frac{d\theta}{dx} - M_z^T. \tag{19}$$

From equilibrium, taking into account the (compressive) applied force, $P$, at both ends, the moment at any position is given by:

$$M = Pw + M_0, \tag{20}$$

where $M_0$ is the moment at $x = 0$.

Differentiating Equations 19 and 20 with respect to $x$ and using Equations 8 and 11 with the additional assumption that the shear angle is small, so that $\sin\gamma_{eq} \approx \gamma_{eq}$ and $\cos\gamma_{eq} = 1$, results in:

$$(EI)_{eq}\frac{d^2\theta}{dx^2} + P\left(\frac{\beta P}{2A\overline{G}}\sin 2\theta + \sin\theta\right) + \frac{dM_z^T}{dx} = 0. \tag{21}$$

As far as the ends (simple supports), we have the moment boundary conditions of:

$$-(EI)_{eq}\frac{d\theta}{dx}(0) - M_z^T = 0; \quad -(EI)_{eq}\frac{d\theta}{dx}(L) - M_z^T = 0. \tag{22}$$

*2.2.1. Linear Analysis*. In the following, we shall linearize the differential equation 21 and derive a closed form and relatively simple solution. This is actually a reasonable approach if we consider the fact that the thermal expansion coefficient $\alpha_l$ is small enough, which means the thermal moment $M_z^T$ influence on the rotation $\theta$ is correspondingly small. Taking into account the fact that the thermal moment, $M_z^T$, is independent of $x$, and using $\sin\ \theta = \theta$, results in the differential equation:

$$(EI)_{eq}\frac{d^2\theta}{dx^2} + P\left(\frac{\beta P}{A\overline{G}} + 1\right)\theta = 0, \tag{23}$$

together with the boundary conditions (22).

If we set:

$$\lambda^2 = \frac{P}{(EI)_{eq}} + \frac{\beta P^2}{(EI)_{eq}A\overline{G}}, \tag{24}$$

then the solution is as follows:

$$\theta(x) = \frac{M_z^T}{\lambda\,(EI)_{eq}}\left[\frac{(1-\cos\ \lambda L)}{\sin\lambda L}\cos\ \lambda L - \sin\ \lambda x\right]. \tag{25}$$

Notice that the symmetry condition $\theta(L/2) = 0$ is satisfied automatically in Equation 25.

The constraint Equation 16, again linearizing, $\cos\ \theta \approx 1$, becomes:

$$\left(N_x^T - P\right)\frac{L}{E_{av}A} - \frac{(M_z^T)^2}{2\left[(EI)_{eq}\lambda\right]^2}\frac{(1-\cos\lambda L)}{\sin\lambda L}\left(\frac{L}{\sin\lambda L} - \frac{1}{\lambda}\right) = 0. \tag{26}$$

The vertical deflection of the beam is obtained for the linear problem by using Equations 8 and 11 and integrating:

$$w(x) = \left(1 + \frac{\beta P}{\overline{G}A}\right)\int_0^x \theta(\xi)d\xi. \tag{27}$$

Substituting Equation 25 gives:

$$w(x) = \frac{M_z^T}{(EI)_{eq}\lambda^2}\left(1 + \frac{\beta P}{\overline{G}A}\right)\left[\frac{(1-\cos\lambda L)}{\sin\lambda L}\sin\lambda L + (\cos\lambda x - 1)\right]. \tag{28}$$

Notice that from Equation 28 the deflections at the ends are zero (as they should), $w(0) = w(L) = 0$, and that the mid-point deflection, $w(L/2) = w_m$, is:

$$w_m = \frac{M_z^T}{(EI)_{eq}\lambda^2}\left(1 + \frac{\beta P}{\overline{G}A}\right)\left[\frac{1}{\cos(\lambda L/2)} - 1\right], \tag{29}$$

and tends to infinity for $\lambda L = \pi$ (the Euler load of the column).

If the thermal loading is prescribed via the fire heat influx, $Q$, then $N_x^T$ and $M_z^T$ can be determined, the only unknown in Equation 28 is $P$ [or $\lambda$ from Equation 24]. Then we can solve the transcendental Equation 26 for $P$ and thus obtain the relationship between the thermal loading, $Q$, and the transverse deflection, $w$. This relationship is obtained for constrained columns only and in this case, $P$, which is obtained from Equation 26, is the support reaction. On the other hand, if the "constraint" condition of immovable supports is released (second case of ends free to move axially), then $P$ is the applied load and the relationship between the mid-point deflection $w_m$ and the applied load $P$ can be obtained from Equation 29. Note also that for zero $M_z^T$, the constraint Equation 26 reduces to $N_x^T = P$, i.e. the solution for a uniformly heated column.

### *2.3. Numerical Results and Discussion*

To illustrate the foregoing analysis, numerical results are presented for a composite column which is exposed to a high heat flux, $Q = 25$ kW/m$^2$. Let us consider two cases, one is the column is constrained and the ends are immovable; the other is that a constant axial compressive load $P$ is applied to the column. The column is shown in Figure 1. Let us assume the entire column of length, $L = 0.15$ m, thickness, $H = 0.012$ m and width $b = 0.025$ m. Case 1 represents the constrained column (immovable ends); case 2 represents the column exposed to the heat flux ($Q$) that is under the constant axial compressive load $P$. The $x$-axis is located at the center of the cross section of the undamaged material in order to simplify the calculation of the thermal buckling analysis by symmetry.

Based on the thermal model/finite element analysis, the temperature and charred layer thickness can be obtained with time. In Figure 2, we show the temperature distribution of the column exposed to a heat flux $Q = 25$ kW/m$^2$ at exposure times from 0 to 280 s. Since only the temperatures at the eight nodes are given, the 7th order polynomial fit curves are obtained by the interpolation, which we can use in the thermal buckling analysis in the future. It is obvious that the temperature increases along with the time $t$. In Figure 3, we show the charred layer thickness variation with time, in which we assume the residual resin content is less than 80%. The variation of residual resin content with time is continuous, however the variation of charred layer thickness is not continuous since if the residual resin content (RRC) is more than 80%, we treated it as the undamaged material; if not, we treated it as the charred material. Thus, the normalized charred layer thickness jumps at the time when the ratio of RRC becomes less than 80%. The variation of the thickness of the charred layer or the undamaged layer is used in

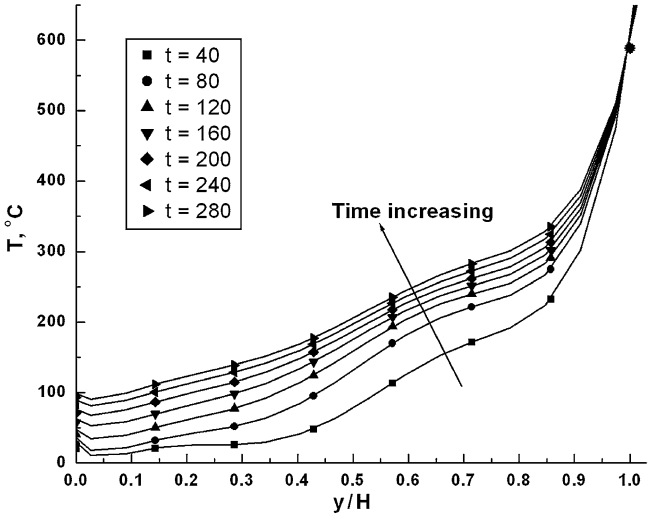


**Figure 2. Temperature distribution in the column subjected to heat flux $Q = 25$ kW/m$^2$, the $y$-axis is normalized by the total thickness of the column. The 7th order polynomial fit curves are obtained by interpolation.**

the quasi-static thermal buckling analysis as follows: The two-layer approximation used treats the undamaged layer as the original material. The temperature distribution in the undamaged region obtained by the thermal/finite element model is used to analyze the thermal resultant force and moment, and the variation of the material properties with temperature is accounted for as well in the calculation. The effect of temperature on the elastic modulus of E-glass/vinyl ester composites is shown in Figure 4. Moreover, since the experimental data are available only up to about the glass transition temperature of the matrix, $T_g$, we assume that beyond $T_g$, if the material is not charred yet, the properties of the material such as Young's modulus and shear modulus do not decrease any more.

With the quasi-static assumption, we analyze the thermal buckling response of the column at exposure times from $t = 0$ s until $t = 300$ s. Obviously, the column is made of two different materials, undamaged (original) layer and charred layer, respectively, which have different material properties as shown in Table 1. The mechanical properties are given at room temperature, which is $T_0 = 20$°C and the original material is E-glass/vinyl ester.

First of all, the thermal moment developed in the column with the exposure time is shown in Figure 5, which is not continuous since the RRC is not continuous. The thermal moment variation is very important, since it shows the influences of the temperature and material properties distributions on the column. At the beginning of the heat exposure, the resin material decomposed due to high temperature and RRC varied with time continuously, but as $t < 80$ s, the RRC is more than 80% for the entire column, therefore we considered no material char-

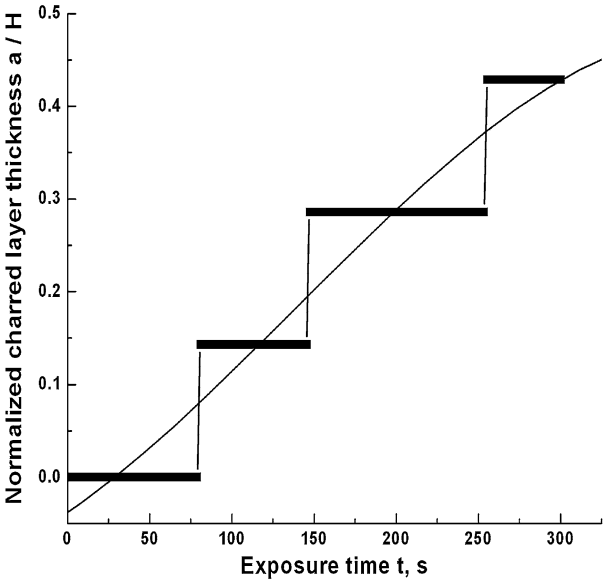


**Figure 3. Normalized charred layer thickness variation with exposure time, which is not a continuous function, due to the assumption that residual resin material less than 80% determines the charred layer thickness. The fire heat flux is $Q = 25\ kW/m^2$.**

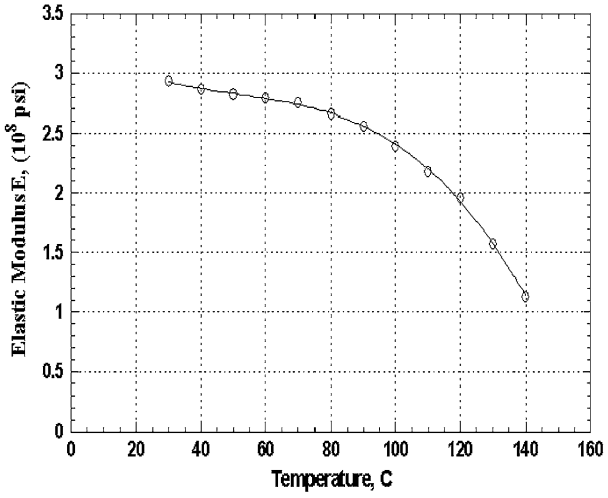


**Figure 4. The effects of temperature on the elastic modulus of E-glass/vinyl ester composites.**

red. The temperature can be determined by the thermal model/finite element analysis; the thermal moment can be obtained from Equation 6 with the known material properties and temperature distributions. It can be seen from the beginning of

**Table 1**
**Material Properties**

| Properties | Parent material | Charred material |
|---|---|---|
| $\alpha_l$, 1/°C | $18.0 \times 10^{-6}$ | – |
| $E_l$, MPa | $20.6 \times 10^{3}$ | – |
| $G_l$, MPa | $2.1 \times 10^{3}$ | – |

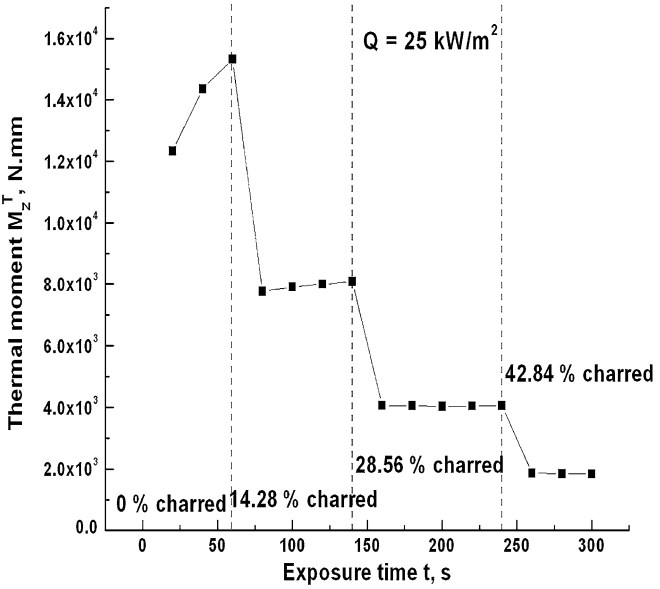


**Figure 5. The thermal moment developed in the column versus exposure time, which is not a continuous function, since the residual resin content does not have a continuous variation with exposure time.**

the heat exposure $t = 0$ s until $t = 60$ s, the thermal moment increased with the exposure time obviously, which is due to the temperature variation development in the column. With the time increasing and from the exposure time $t = 80$ s until $t = 140$ s, part of material (1/7 of the entire thickness of the column) is charred based on the Figure 3, the properties of the charred material are neglected; the thermal buckling response of the remaining material is determined. The absolute value of the thermal moment decreased a lot in this time zone; the decreasing of thickness of the column and the variation of the temperature resulted in the decreasing of the thermal moment; subsequently the moment did not change too much between 75 s and 140 s compared with the beginning of the heat exposure from $t = 0$ s until $t = 60$ s. Similarly, with the exposure time increasing further, more material is charred and the thermal moment decreased further.

We show the axial constraint stress $\sigma_{xx}$ in Figure 6; the column is pinned at both ends, which are immovable, and is subjected to a heat flux $Q = 25$ kW/m$^2$. The axial constraint stress is determined at different exposure time from $t = 20$ s until $t = 300$ s with the quasi-static assumption. It is obvious that the axial constraint stress increases with time $t$ as $t < 140$ s, but $\sigma_{xx}$ decreases with exposure time as $t > 140$ s; the 2nd order polynomial curve was obtained to fit the variation trend approximately. We can analyze the variation of the axial constraint by dividing the exposure time into four zones, the thickness of charred material being constant in each zone (the definition of each zone can refer to Figure 3). We can see that the variation of the constraint stress is non-linear in each zone, which is due to the material properties, which decrease with the exposure time nonlinearly. For the entire exposure time, there exists a peak value of the axial constraint stress at exposure time $t = 140$ s. After that, $\sigma_{xx}$ decreases, which is coming from the fact that the ends are restrained; therefore, beyond a certain level of deformation, the structure starts to "pull" from the ends rather than "push" against the ends.

Based on the axial support force obtained, the deformation of the column can be determined from Equation 28. We show the deformation of the constrained column at different exposure times in Figure 7. It is obvious that the deformation increases with the exposure time from $t = 60$ s until $t = 300$ s. Actually, the increasing of the deformation before $t = 120$ s is smaller than that of the defor-

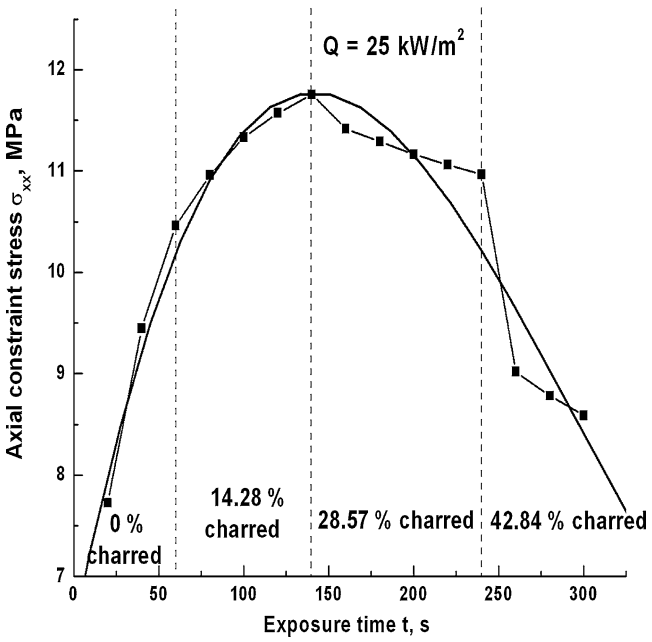


**Figure 6. The axial constraint stress $\sigma_{xx}$ versus exposure time *t*. A 2nd order polynomial curve was obtained to fit the variation trend.**

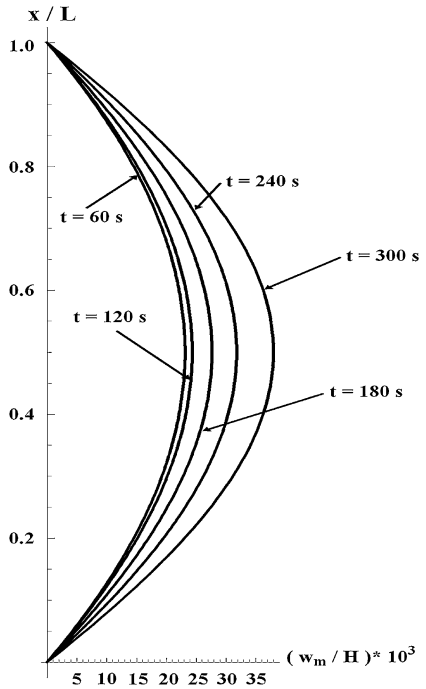


**Figure 7. The deformation of the constrained column under the heat flux $Q$ = 25 kW/m$^2$ due to fire, at different exposure times.**

mation after $t$ = 120 s. The reason for that is coming from the decreasing of the bending rigidity, $EI_{eq}$, which is strongly associated with the thickness of the column. With increasing the heat exposure time, the thickness of the column decreases due to the resin material decomposition, which results in the decreasing of the bending rigidity $EI_{eq}$, therefore the column bends more with even lower thermal bending moment. The mid-point deflection $w_m$ normalized by the original thickness of the column is shown in Figure 8. The variation of the mid-point deflection is not smooth, however the linear curve can be obtained to fit it approximately. It can be seen that the mid-point deflection of the column increases in general with the exposure time. Since the direction of the mid-point deflection is always positive, this means that the column bends toward the heat source under the constrained boundary conditions. In the experimental study reported in the subsequent section, a positive deflection can be observed in the tests for the column exposed to the heat flux $Q$ = 25 kW/m$^2$ under the constant compressive axial load, $P$, corresponding to a stress of 10.5 MPa (based on the original section). The failure of the column in this test can be seen in Figure 9.

Figure 10 presents a plot of the axial support force $P$ versus the mid-point deflection $w_m$ for different exposure times. In each case, the mid-point deflection $w_m$ was calculated from the linear analysis for the pinned column under the external heat

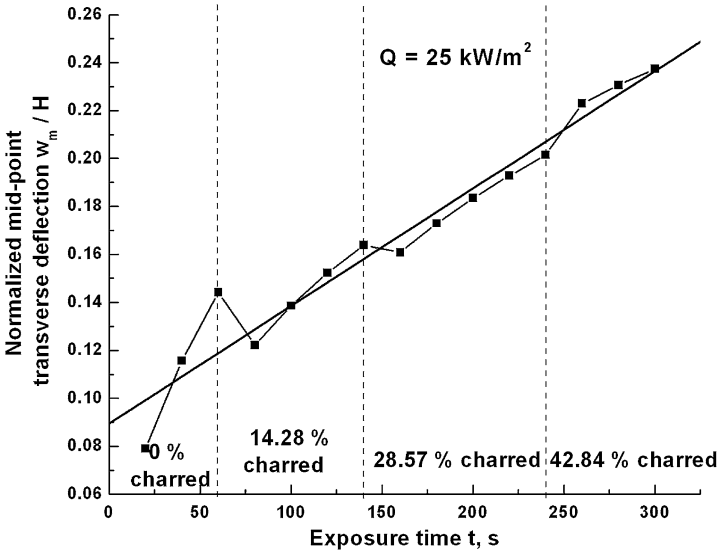


**Figure 8. The normalized mid-point transverse deflection versus exposure time for the constrained column under the heat flux due to fire, $Q$ = 25 kW/m$^2$.**

**Figure 9. The failed fiberglass reinforced composite column exposed to the fire heat flux $Q$ = 25 kW/m$^2$ under the constant axial compressive load, $P$, corresponding to a stress of 10.5 MPa (based on the original section).**

flux and the end of the column was free to move, so the constraint condition shown in Equation 26 is not applicable. The solution of the problem is in Equation 28 and the variation between the axial force $P$ and the mid-point deflection $w_m$ can be obtained from Equation 29. Figure 10 shows that, at the beginning of the heat exposure, the axial force $P$ increases initially with only a small bending deflection; but as $P$ approaches the classical buckling load, $P_{Euler}$, the transverse deflection

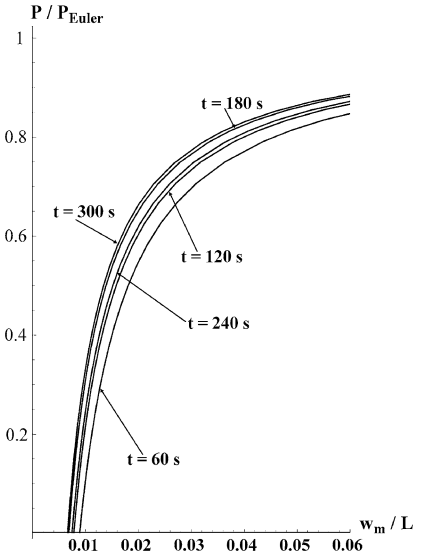


**Figure 10. Axial force vs mid-point deflection for a pinned beam with external fire heat flux $Q = 25$ kW/m$^2$ at different exposure times; the axial force and the mid-point deflection are normalized by the Euler buckling load, $P_{Euler}$, and the length of the column L, respectively. The ends of the columns are free.**

then increases rapidly. The column behaves much like an "imperfect" column. Eventually, in all cases, the axial support force approaches $P_{Euler}$ as the mid-span deflection becomes large. The temperature change through the thickness has effectively an analogous role for an axially restrained column, as that of an imperfection on a mechanically loaded column.

## *2.4. Experimental Developments*

Although the mechanical behavior of polymeric composites during fire and post-fire has been investigated [11], very little information is available concerning the more realistic situation of simultaneous mechanical loading and fire exposure. In a pioneering study, Gibson et al. [14] investigated the effect of compressive and tensile loading on the failure time of composite specimens subjected to surface heat fluxes between 25 kW/m$^2$ and 75 kw/m$^2$. For a 0/90 fiberglass reinforced vinyl-ester matrix, the time-to-failure was found to be strongly influenced by the heat flux intensity and the applied load level.

The goal of the present experimental investigation was to characterize the compressive mechanical response, failure mode and time-to-failure for a fiberglass-reinforced polymeric composite simultaneously exposed to high heat flux and compressive axial loading. The experiments utilized a specially modified cone calorimeter that permitted direct mechanical loading of samples during simultaneous

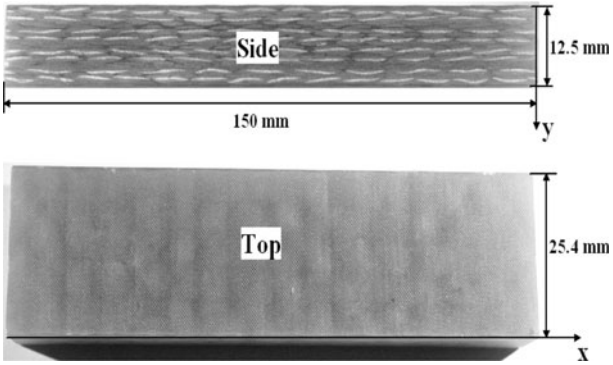


**Figure 11. Test coupons with [(0/90/45/-45/)$_S$] ply lay-up machined from a twenty ply composite panel with a nominal thickness of 12.5 mm. The top and bottom surfaces were left in the as-processed condition. The x–y coordinates refer to the axial and thickness directions.**

exposure to heat fluxes of 25 kW/m$^2$, 50 kW/m$^2$ and 75 kW/m$^2$. In order to analyze the response of the test samples and compare the experimental data with theoretical results, the axial displacement and mid-point transverse deflection were measured. Many of the test data presented herein are from Liu and Holmes [15].

## 2.5. *Material, Specimen Geometry and Grips*

*2.5.1. Test Sample Geometry*. A fiberglass-reinforced vinyl-ester (Derakane 510A) composite laminate was used in the experiments. The laminate panels were manufactured with twenty plies (Seemann Composites Inc., Gulfport, MS) in the form of flat 24-inch × 24-inch panels. The 12.5 mm thick panels had a [(0/90/45/-45/)$_S$] ply lay-up. Test coupons (see Figure 11) were machined dry from the panels using carbide tooling. Two different specimen lengths, 150 mm and 100 mm, were utilized in the experiments. In both cases, the nominal thickness was 12.5 mm and the width was 25.4 mm. The broad (25.4 mm wide) faces of the specimens, one of which was exposed to the heat source, were left in the as-processed condition.

The ends of the composite specimens fit into flat-bottom cavities that were machined by EDM into Inconel 718 alloy grips. Each grip had a fixed cavity depth of 25 mm. For the shorter 100 mm long specimens, inserts were placed in the grip cavities to fix the heated length of the specimens to 74 mm. For the 150 mm long specimens, the distance between grip faces was 100 mm (this corresponds to the heated length of the specimen); for the 100 mm long specimens the distance between grip faces was 74 mm.[1] In order to minimize heat loss from the specimen to the grips, the surfaces of the specimens located within the grips were insulated with a thin ceramic layer (Zircar Inc., Alumina Cement) approximately

[1]100 mm was the maximum length over which uniform heating could be obtained in the cone calorimeter.

0.4 mm thick. IN-718 shims between the sides of the specimen and grip cavity were used to firmly fix the specimen within the grips and minimize any transverse specimen movement in the grips. The grips approximated clamped end-conditions for axial loading.

### 2.6. Experimental Apparatus

*2.6.1. Heat Source.* A cone-calorimeter equipped with a 5000 W electric cone heater was used as the heat source for the simulated fire tests (Fire Testing Technology Limited, West Sussex, U.K.). The cone calorimeter and modifications used to allow simultaneous mechanical loading are shown in Figure 12 (details of the loading module design are provided below).

In a cone calorimeter, the heat flux is applied to only one surface of a test specimen. The exit diameter of the cone heater was 158 mm. For this exit diameter and cone design, uniform heat fluxes as high as 100 kW/m$^2$ were possible over a

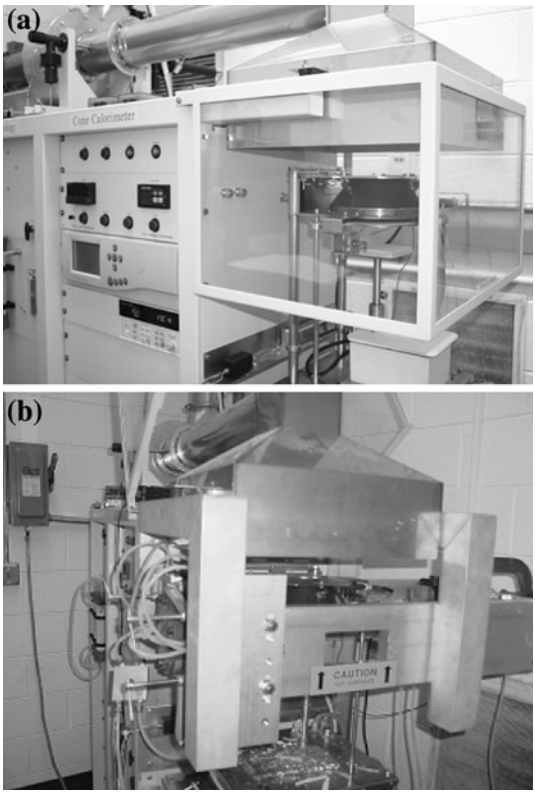


**Figure 12. (a) Cone calorimeter before modifications to allow simultaneous mechanical loading; (b) Calorimeter after installation of pneumatic loading fixture for combined fire and compression testing (Liu and Holmes [15]).**

100 mm × 100 mm surface area. In the present investigation, the region of uniform heating limited the maximum length of test specimens to 100 mm. Although larger specimen widths were possible, a 25.4 mm specimen width was chosen to reduce the size of the test fixtures and actuator used to apply axial compressive loads. To minimize heating of the specimen sides, a thin (0.3–0.4 mm thick) alumina ceramic layer was applied to both sides of the specimens (along the 12.5 mm faces). In an initial study, performed to determine the effect of surface insulation on failure time, several experiments were conducted with 150 mm long specimens with and without surface coatings on the unheated specimen face. These trial experiments showed that coating the backside of the specimens did not significantly affect failure time or failure mode. Therefore, all remaining experiments discussed in this paper were performed with the specimens coated only on their sides and along the surfaces located within the loading grips.

For all tests, the distance between the exit of the cone heater and the specimen surface was maintained at 25 mm. The applied heat flux was varied from 25 kW/$m^2$ to 75 kW/$m^2$ to simulate the surface heating expected for fires ranging from small to large intensity. Prior to testing, a heat flux meter was used to measure the heat flux at the surface of the specimens.

*2.6.2. Loading Module.* To investigate the effect of simultaneous mechanical loading on the compressive behavior of the composite laminate, a load frame with pneumatic actuator was designed to fit directly beneath the cone heater (Figure 13). A close up of the specimen and grip arrangement is shown in Figure 14a. A load cell mounted at one end of the load frame was used to monitor the specimen load level (Figure 14b). To minimize transverse and axial deflections that can occur with low stiffness load cells, a load cell with very high axial and lateral stiffness was utilized (110 kN capacity, Interface Inc., Model # 120AF-25 K). The grip at one end of the specimen was rigidly attached to a load cell. The grip at the opposite end of the specimen was attached to an aluminum H-block that was mounted to a linear bearing system; this arrangement permits axial motion only (see Figure 14c). An LVDT was used to measure the axial displacement of the specimen. The tip of the LVDT was in contact with the cold-end of the H-block. For several of the tests, an additional LVDT was used to measure the mid-point transverse deflection of the unexposed surface of specimen.

*2.6.3. Test Procedure and Influence of Surface Insulation.* After bringing the cone heater to the desired temperature and allowing it to stabilize for 30 min, the exit shutters were closed. A specimen (with attached grips) was then installed into the loading module and the specimen was loaded to the desired load level. Within 10 s of applying the load, the shutters shielding the test specimen from the heat source were quickly opened. Compressive loads of 1.11 kN (250 lb) to 3.34 kN (750 lb) were used in the experiments; these load levels provided nominal compressive stresses between 3.5 MPa and 10.5 MPa. The tests were performed using surface heat fluxes of 25 kW/$m^2$, 50 kW/$m^2$ and 75 kW/$m^2$. During the experiments, the axial displacement of the specimen, load level and elapsed time were continuously recorded until specimen failure (data was gath-

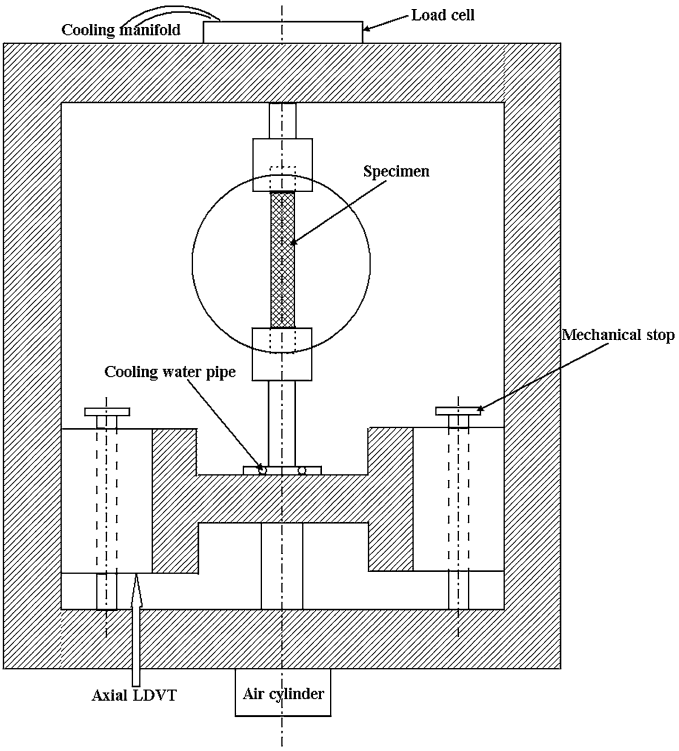


**Figure 13. Schematic of loading module used to mechanically load specimens during fire exposure in the cone calorimeter. The LVDT shown was used to measure axial displacement of the test specimens. The cooling manifold is used to keep the linear bearings and the load cell at constant temperature (Liu and Holmes [15]).**

ered using an 18-bit data acquisition board). When the specimens failed, the H-block hit the mechanical stops (see in Figure 14c) to limit complete collapse of the specimens, which would obscure the failure modes. After specimen failure, the shutters were immediately closed and the specimen removed from the loading fixture. All experiments were videotaped to document the failure mode of the specimens. The time-to-failure of specimens was documented by a timer on the cone calorimeter and was further verified by examination of the videotape of each test.

## 2.7. *Experimental Results*

*2.7.1. Influence of Surface Heat Flux and Stress Level on Failure Time.* The time-to failure data for all specimens are summarized in Table 2. Failure times were readily determined since all specimens exhibited catastrophic collapse. Analysis of the video recordings from the experiments showed that, for all specimens, the final failure event was exceedingly rapid (the transition from an intact, load bearing

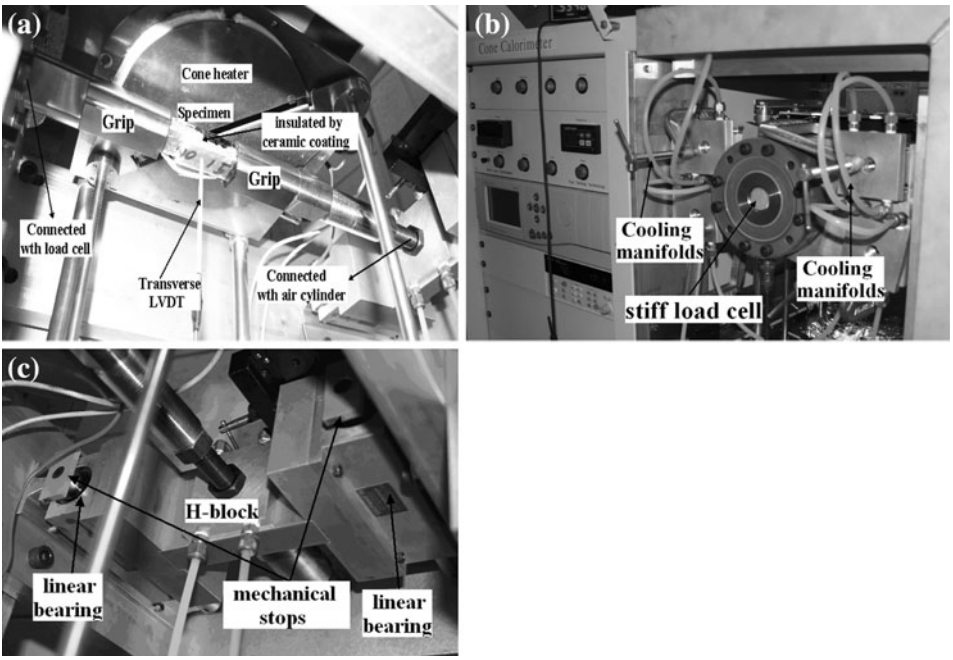


**Figure 14. (a) A Close up of specimen and grip arrangement used for the combined fire and compression testing; (b) A load cell mounted at one end of the load frame was used to monitor specimen load level; (c) H-block and linear bearings races, which are used to constrain deformation to the axial direction only (Liu and Holmes [15]).**

**Table 2**
**Time-to-Failure ($t_f$) of Fiberglass-Reinforced Vinyl-ester Composites Under Simultaneous Surface Heating and Axial Compressive Loading. At 50 kW/m$^2$, Heated Specimen Lengths of 100 mm and 74 mm were Studied**

| | | Axial compressive stress, MPa | | | |
|---|---|---|---|---|---|
| Heat flux (kW/m$^2$) | | 3.5 | 5.25 | 7.0 | 10.5 |
| 25 | | $t_f$ = 2549 s | $t_f$ = 660 s | $t_f$ = 366 s | $t_f$ = 251 s |
| 50 | 100 mm | 404 | 242 | 178 | 131 |
| 50 | 74 mm | 385 | 207 | 133 | 117 |
| 75 | | 191 | 171 | 123 | – |

specimen, to catastrophic collapse was less than 50 ms). For a heat flux of 25 kW/m$^2$, failure times ranged from approximately 2549 s at 3.5 MPa to 251 s at 10.5 MPa. At 50 kW/m$^2$, failure times were considerably shorter, 404 s at 3.5 MPa and 131 s at 10.5 MPa. For the highest heat flux used, 75 kW/m$^2$, failure times were much shorter, 191 s at 3.5 MPa and 123 s at 7.0 MPa.

As shown in Figure 15, the relationship between time-to-failure and axial applied load is nonlinear, and the slope of the curve decreases with increasing compressive load. The non-linear variation is most likely caused by char formation and degradation of the material properties. The rate of char formation decreases with increasing exposure time since the char layer influences the transport rate of oxygen to the combustion front and, because of its lower thermal conductivity, reduces heat conduction to the uncharred material [11, 14].

*2.7.2. Failure Mode*. The failure modes of the 150 mm long and 100 mm long specimens were significantly different and for convenience are discussed separately below.

*150 mm samples*. The 150 mm long test samples (100 mm heated length) failed by global buckling. Figure 16 show the failure modes of specimens exposed to different heat fluxes under the applied axial loads from 1.11 kN (250 lb) to 3.34 (750 lb), respectively. It is interesting to note that for only two of the specimens, the undamaged side of the specimen bent towards the heat (see Figure 16). For all

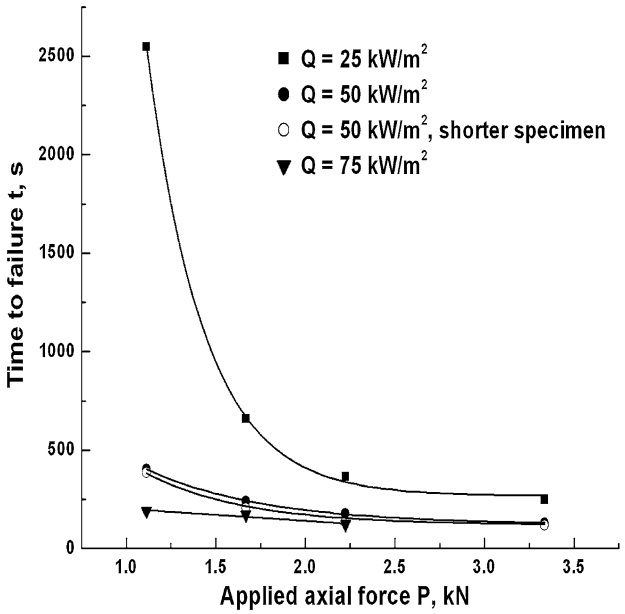


**Figure 15. Relationship between the time-to-failure and compressive axial force for specimens subjected to single-sided heat flux levels of 25 kW/m², 50 kW/m² and 75 kW/m². Two specimen lengths were used: 150 mm (100 mm heated length) and 125 mm (74 mm heated length). For all heat fluxes, the slope of the time-to-failure versus axial force increases with decreasing force *P* (Liu and Holmes [15]).**

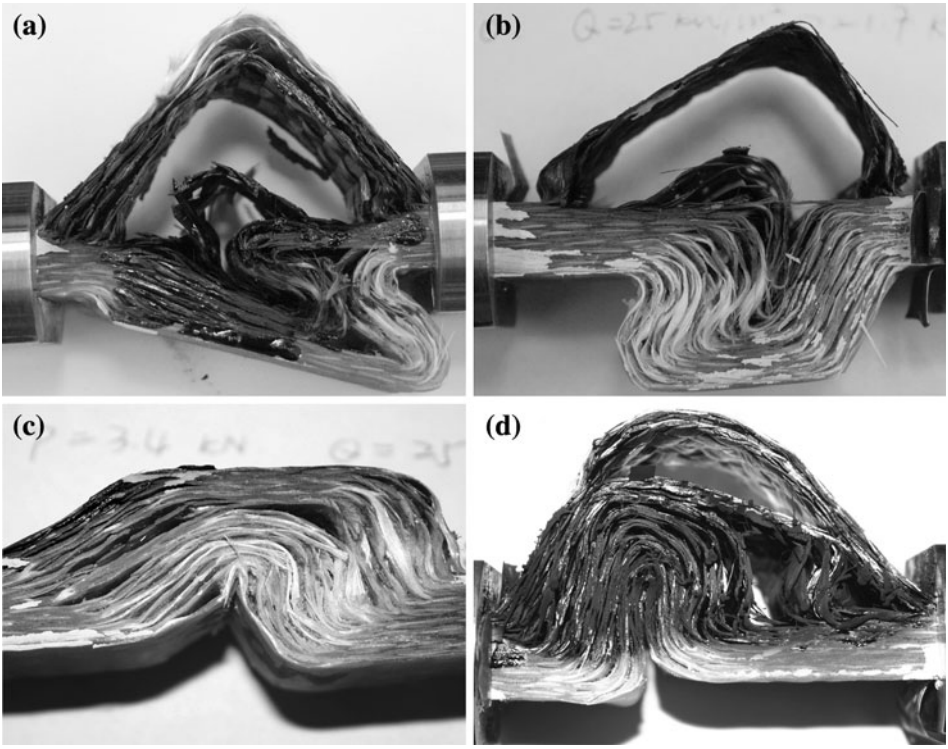


**Figure 16. Digital images showing failure modes of 150 mm long specimens (100 mm heated length between grips) for various thermal and axial compressive loads; (a) 50 kW/m$^2$ and compressive load of 1.11 kN (250 lb); (b) 25 kW/m$^2$ and compressive load of 1.66 kN (375 lb); (c) 25 kW/m$^2$ and compressive load of 3.34 kN (750 lb) and (d) 75 kW/m$^2$ and compressive load of 2.224 kN (500 lb). All specimens failed by global buckling and failure occurred in an unexpected catastrophic fashion (Liu and Holmes [15]).**

other tests, the unexposed side of the specimen deflected away from the heat source (e.g., Figure 16).

The buckling instability occurred in an unexpected catastrophic fashion. As noted earlier, the final instability and collapse was, for all practical concerns instantaneous, occurring in less than 50 ms (determined by examination of videos). Prior to failure the amount of transverse deflection was very limited but increased dramatically at the onset of failure. The catastrophic buckling collapse of specimen observed during combined thermal and compressive loading was much different than that found by Liu et al. [16] in earlier post-fire compression testing of the same composite. In the post-fire compressive study, specimens were subjected (without load) to similar heat flux intensities, during post-fire monotonic compression testing, specimens failed by progressive delamination with a gradual increase in transverse deflection until specimen failure.

There are several possible mechanisms for the sudden buckling failure under combined thermal and mechanical loading: (1) material property degradation at high temperatures, (2) delamination growth between the laminate plies and (3) the presence of a thermal bending moment. Since the gripping arrangement and loading module are very rigid and motion is constrained to the axial direction, the axial deformation due to the external compressive load should be distributed uniformly over the specimen cross section. With this boundary condition, the axial load $P$ would act along the neutral axis of the specimen and the stress distribution caused by the external force $P$ will not generate a mechanical moment although the material properties distribution is not uniform along the thickness direction during the tests. However, since the temperature and material properties such as Young's modulus are non-uniform along the thickness of the specimen, a thermal moment can develop from the onset of testing [17]. The resultant moment can be expressed in the form $\int_A E_l \alpha_l \Delta T(y - e)dA$, where $e$ is the eccentric distance between the geometric center and the neutral center of the cross section (if we assume as an approximation isotropic behavior), $A$ is the area of the cross section, and $y$ is the coordinate along the thickness direction (see Figure 11). Young's modulus $E_l$ and the temperature $T$ are non-uniform along the thickness and a function of the coordinate $y$; $\alpha_l$ is the thermal expansion coefficient along the axial direction $x$ of the specimen.

*100 mm Samples*. For the 100 mm long test specimen (74 mm heated length between grips faces), the failure mode, involving kinking of fibers, was significantly different compared to the longer specimens. Figure 17 compares typical failure modes for 150 mm and 100 mm long specimens that were exposed to a heat flux 50 kW/m$^2$ and an applied axial load of 2.22 kN (500 lb).

With less char formation in the shorter specimens, and significantly less transverse displacement than found with the longer specimens discussed above, global buckling does not occur; instead, the samples failed by local kinking of the glass fiber tows. This failure instability occurs rapidly without warning (i.e., there were no obvious changes in specimen appearance or axial/transverse deflection until the failure event initiated). A similar kinking failure mode was observed for unexposed material (removed from the same panel) during monotonic compressive loading at room temperature. At room temperature the failure load of 100 mm long specimens with the same cross sectional area was 94.3 kN—see Figure 17c).

One further comment about failure modes can be made. Namely, for a heat intensity of 25 kW/m$^2$, the char layer thickness was comparable to that found for shorter specimens exposed at a higher heat flux (see Figure 18). Yet, the failure modes for a similar char layer thickness were much different, suggesting that the failure mode is not directly related to char layer depth but is intimately related to specimen length and therefore stress state and the magnitude of the thermally generated bending moment.

*2.7.3. Axial Displacement*. Figure 19 shows the axial displacements of specimens exposed to a heat flux of 25 kW/m$^2$ under constant compressive loads from 1.11 kN (250 lb) to 3.34 kN (750 lb). The initial displacement is from elastic deforma-

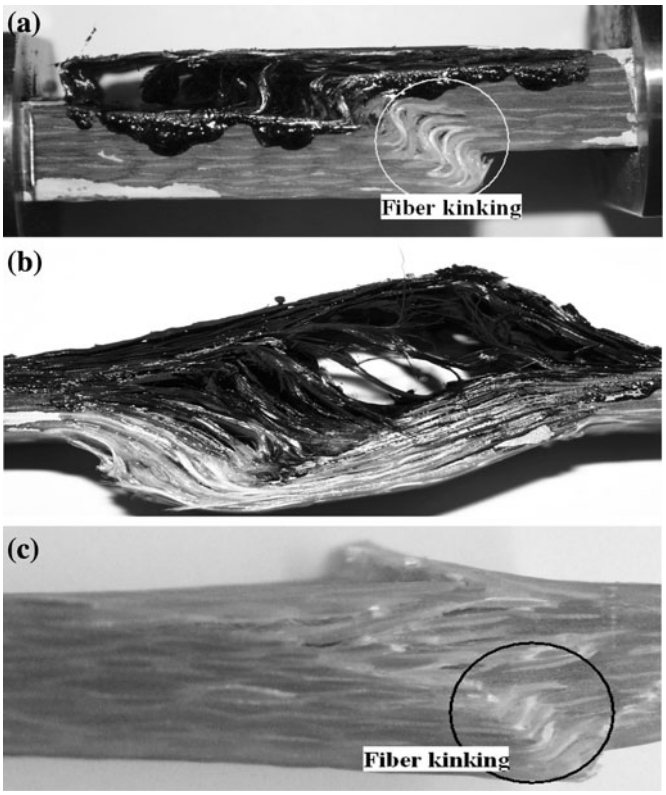


**Figure 17. Digital images comparing failure modes of 150 mm and 100 mm specimens tested at the same heat flux intensity of 50 kW/m$^2$ and compressive load of 2.22 kN (500 lb). (a) 125 mm specimen. (b) 150 mm specimen. (c) Fiber kinking in a specimen without heat exposure and tested to failure under a monotonically increasing compressive load at room temperature (for this specimen the failure load was 94.3 kN (21199 lb).**

tion prior to heat exposure. Immediately after exposure to the heat source, thermal expansion of the specimen causes an increase in specimen length (axial strain becomes more positive). A similar phenomenon has been observed in tests performed by Bausano et al. [18]. The decrease in compressive displacement continued until the temperature induced char formation and stiffness loss overcame the effect of thermal expansion. From Figure 19, we can see the influence of constant compressive load on the axial displacement for the same heat flux intensity. In order to explain the variation of the axial compressive displacement versus axial load, a simple 1D model, in which we do not consider transverse deflection, can be used.

The thermal force can be written in a format similar to that of Equation 5:

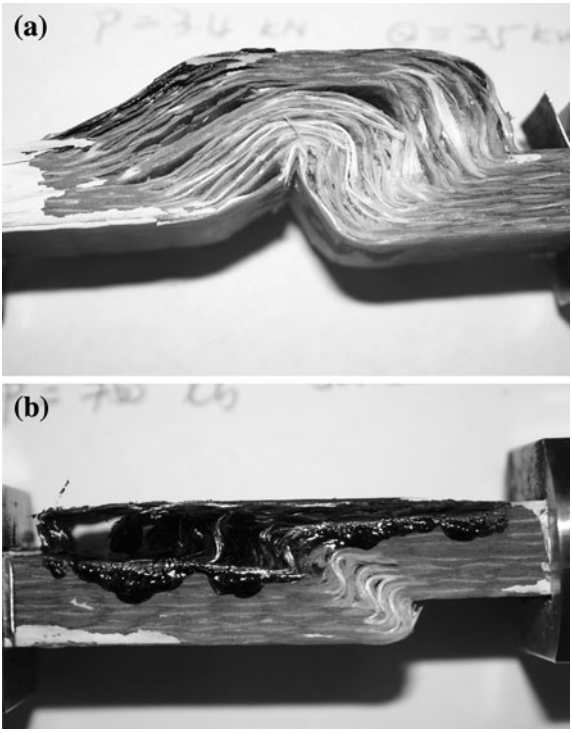


**Figure 18. (a) Digital image showing failure mode of 150 mm long specimen exposed to 25 kW/m$^2$ and compressive load of 3.34 kN (750 lb); (b). Digital image showing failure mode of 100 mm long specimen exposed to 50 kW/m$^2$ and a compressive load of 3.34 kN (750 lb). The charred layer thickness is similar for these two specimens, but the failure modes are different.**

$$N_x^T = \int_A E_l(t,y)\,\alpha_l\,\Delta T(t,y)dA. \tag{30}$$

The total axial force applied at the neutral axis is

$$N_x = P - N_x^T = P - \int_A E_l(t,y)\alpha_l\,\Delta T(t,y)dA. \tag{31}$$

Thus, the axial strain is written as:

$$\varepsilon_x = \frac{N_x}{AE_{av}(t)} = \frac{P - \int_A E_l(t,y)\,\alpha_l\,\Delta T(t,y)dA}{AE_{av}(t)}, \tag{32}$$

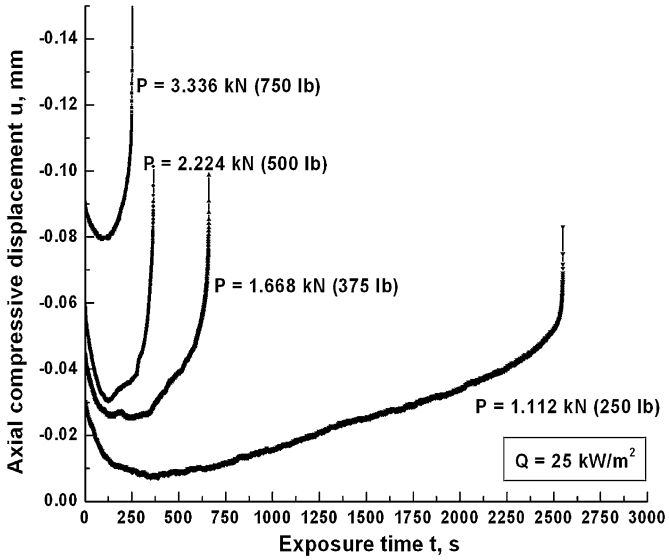


**Figure 19. The axial displacements of specimens exposed to the heat flux 25 kW/m$^2$ under the constant compressive loads from 1.112 kN (250 lb) to 3.336 kN (750 lb). The initial compressive load decreased due to thermal expansion and later the increasing of the axial displacement is due to the material stiffness loss (Liu and Holmes [15]).**

where $E_{av}$ is the longitudinal average modulus, which can be expressed as $E_{av} = \int_A E_l(t,y)dA$, where $A$ is the area of the cross section of the specimen. $\Delta T$ is the difference between the average temperature of the specimen and room temperature.

Both $E_{av}$ and $\Delta T$ are functions of exposure time. If the thermal force and the total axial strain $\varepsilon_x$ do not vary with the axial position, the total axial displacement $u_x$ can be written as:

$$u_x = \int_0^L \varepsilon_x dx = \frac{[P - \alpha_l \int_A E_l(t,y)\Delta T(t,y)dA]L}{AE_{av}(t)} = \frac{PL - \alpha_l(\int_A E_l(t,y)\Delta T(t,y)dA)L}{AE_{av}(t)}$$

$$= \frac{PL}{AE_{av}(t)} - \frac{\alpha_l(\int_A E_l(t,y)\Delta T(t,y)dA)L}{AE_{av}(t)}. \tag{33}$$

The first term in Equation 33 is associated with the mechanical response of the specimen to the external applied force $P$; the second term is associated with the

thermal force, which is dependent on the heat flux intensity and exposure time. If the specimen is exposed to the same heat flux with the same heat exposure time, and we make a simplifying assumption that the material degradation in material properties is associated with heat intensity and exposure time only, the material response is independent of loading history, we would expect the axial displacement $u_x$ to be linearly related to the applied force, $P$. With this assumption, the slope can be written as $s = \frac{L}{E_{av}(t)A(t)}$, which is dependent only upon heat flux and exposure time and is not a function of the applied load.

In Figure 20, the axial displacement $u_x$ versus applied compressive load is plotted under a heat flux of 50 kW/m$^2$ at exposure times from 5 s to 30 s. During the initial stages of heat exposure (e.g., 5 s and 10 s in Figure 20) the axial displacement is linearly related to the applied load $P$. The slope is dependent on the material longitudinal average modulus $E_{av}$, which is associated with heat flux intensity and exposure time; the decrease in axial compressive displacement is caused by thermal expansion of the specimen (note that the pneumatic loading actuator allows axial displacement while maintaining a constant load). The slope between the axial displacement and the axial load was the same, which means the average modulus $E_{av}$ did not change very much. Examination of Figure 20 also shows that for all load levels from 1.11 kN to 3.34 kN, the axial compressive displacement change at the start of the tests was the same (e.g., 5 s and 10 s in Figure 20), which means that the displacement change due to thermal expansion for all specimens under different axial compressive loads was the same. The two curves indicate that the material stiffness did not change significantly at the beginning of heat

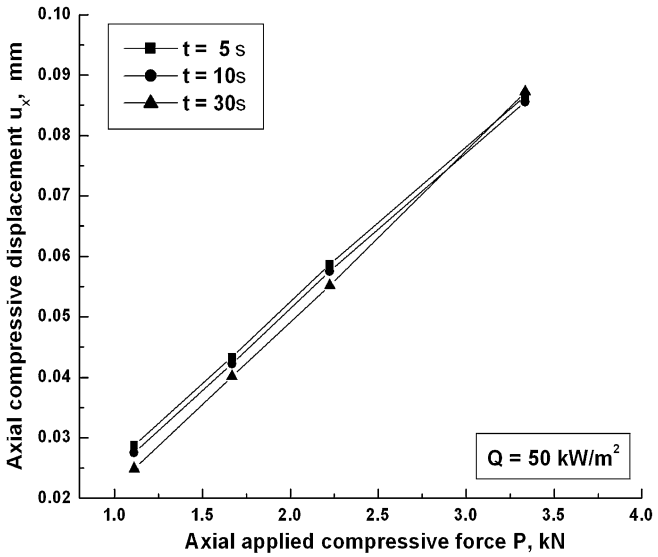


**Figure 20. The axial compressive displacement $u_x$ versus the axial applied compressive $P$ under the same heat flux 50 kW/m$^2$ with different heat exposure time from 5 s to 30 s.**

exposure since the slope did not change very much as mentioned above. As the heat exposure time increased further ($t$ = 30 s in Figure 20), the relationship between axial displacement and applied load is no longer linear; the slope increased with load, indicating a further decrease in material stiffness with increasing load. This result suggests that material stiffness loss is dependent not only upon heat flux intensity and heat exposure time, but also upon the applied load $P$. This effect is verified further in Figure 21, which shows the axial compressive displacement $u_x$ versus compressive load for heat exposure times from 5 s to 100 s.

At 5 s, the relationship between axial displacement and axial load is linear; at an exposure time of 100 s, the relationship is not linear and the slope varies significantly with external applied load. The slope increased with increasing axial compressive load. Thus, the simplifying assumption made in Equation 33, that the slope between the axial compressive displacement and the axial compressive load is dependent only on the heat flux intensity and heat exposure time, is an over simplification. There are several possible reasons for the interrelation between heat flux, heat exposure time and applied external load:

(a) the char formation and depth is influenced by load level;
(b) a thermal moment exists and increases with load level and
(c) the extent of delamination is influenced by load level.

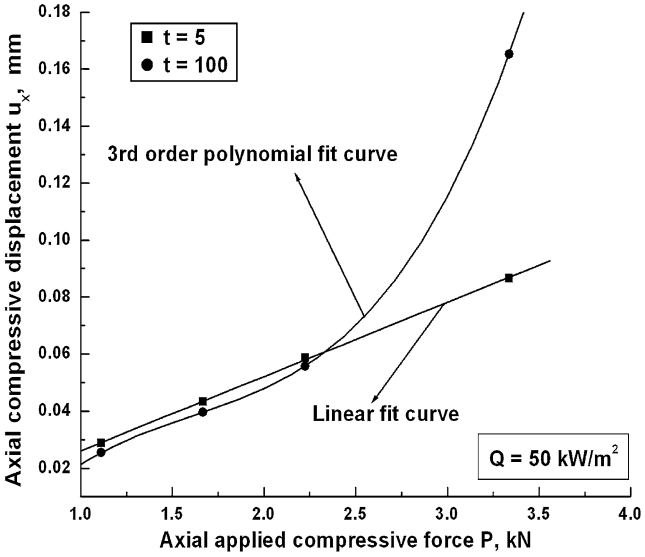


**Figure 21. The axial compressive displacement $u_x$ versus the axial applied compressive $P$ under the same heat flux 50 kW/m$^2$ with different heat exposure time 5 s and 100 s. At an exposure time of 5 s, the relationship between the axial displacement and axial load is linear; at 100 s, the relationship is non linear and the slope is dependent on $P$.**

Of these, it is thought that delamination growth between the laminate plies is the most important mechanism. Under higher loads, delamination growth accelerates the loss in material stiffness. To gain insight into the mechanisms responsible for the observed axial displacement and failure modes, it is instructive to model the relationship between the axial compressive displacement $u_x$ and the axial compressive load $P$ in Figure 19. As an approximation, a 1D model can be used to relate the specimen displacement to the temperature change $\Delta T$, average material modulus $E_{av}$ and the char depth.

## 3. Conclusions

The response of a composite column exposed to a heat flux due to fire and under an axial compressive load is studied. Theoretical and experimental works are included in this paper. For the theoretical part, two cases are considered: (a) when the column is axially restrained (immovable ends) and (b) when the ends are free to move axially (no axial restrain) and an axial force is applied. First, the temperature and charred thickness distribution are obtained by the thermal/finite element method of Gibson et al. [8], which solves the heat response problem for the polymer composite material. Subsequently, this temperature and charred thickness profile are used in conjunction with the temperature-dependent moduli of the composite residual resin layer to obtain the buckling response; in this phase the mechanical properties of the char layer are neglected. In addition, the thermal buckling analysis includes the effect of transverse shear.

The effect of simultaneous axial compressive loading on the time-to-failure and failure mode of a vinyl-ester/fiberglass composite exposed to single-sided surface heat fluxes between 25 kW/m$^2$ and 75 kW/m$^2$ was examined in the experimental work. Two different length specimens were used in the study; the shortest samples had a heated length of 74 mm and the longest samples had a heated length of 100 mm. Based upon the results, the following conclusion can be made:

1. Due to the resin material decomposition and charred layer thickness increasing with time, the thermal moment induced in the column decreased significantly.
2. The variation of the axial constraint stress with the exposure time is non-linear for the constrained column; there exists a peak value and after that, the axial constraint stress decreases. The reason for this variation is coming from the variation of the char thickness and the non-linear temperature and material properties distributions in the undamaged composite.
3. The mid-point deflection for the constrained column increases with heat exposure time (approximately in a linear fashion), and the bending deformation is toward the heat source, which is consistent with the experimental observation for the similar column.
4. For the column under heat exposure, which is free to move axially (unconstrained case), the response is similar to that of an imperfect column. The temperature distribution through the thickness has effectively a role analogous to that of an imperfection on a mechanically loaded column.

5. For the range of heat fluxes and compressive stresses (3.5 MPa to 10.5 MPa) studied, all specimens exhibited catastrophic compressive collapse. Global buckling was observed for the specimens with a heated length of 100 mm. Failure occurred by local fiber kinking for the shorter specimens with 74 mm heated length.
6. For both specimen lengths, the relationship between time-to-failure and axial applied load was non-linear. For specimens with a heated length of 100 mm, at a heat flux of 25 $kW/m^2$ the failure time ranged from 2549 s at 3.5 MPa to 251 s at 10.5 MPa. At 75 $kW/m^2$, the highest heat flux studied, the failure time of the same specimens ranged from 191 s at 3.5 MPa to 123 s at 7.0 MPa. The total time-to-failure of the shorter specimens was slightly less than that of the longer specimens. For specimens with a heated length of 74 mm, the failure times were 117 s at 10.5 MPa and 385 s at 3.5 MPa under a heat flux exposure of 50 $kW/m^2$.
7. The char layer thickness for the shorter specimens was considerably less than that of the longer specimens. It is not known if the difference in char layer thickness is related to the stress state or a different temperature distribution on the test samples;
8. There exists the thermal bending moment for all specimens, which causes out-of-plane transverse deflection from the onset of heat exposure. The thermal moment has more influence on the response of the longer specimen than that of the shorter specimen.
9. Material stiffness loss is dependent not only on the heat flux intensity and heat exposure time, but also on the level of applied compressive load.

## Acknowledgments

The financial support of the Office of Naval Research, Grant N00014-03-1-0189, and the interest and encouragement of the Grant Monitor, Dr. Luise Couchman, is gratefully acknowledged.

## References

1. Sorathia U, Rollhauser CM, Hughes WA (1992) Improved fire safety of composites for naval applications. Fire Mater 16:119–125
2. Sorathia U, Lyon R, Gann R, Gritzo L (1996) Materials and fire threat. SAMPE J 32:8–15
3. Egglestone GT, Turley DM (1994) Flammability of GRP for use in ship superstructures. Fire Mater 18:255–260
4. Scudamore MJ (1994) Fire performance studies on glass-reinforced plastic laminates. Fire Mater 18:313–325
5. Brown JR, Mathys Z (1997) Reinforcement and matrix effects on the combustion properties of glass reinforced polymer composites. Composites 28A:675–681
6. Mouritz AP, Gardiner CP (2002) Compression properties of fire-damaged polymer sandwich composites. Composites 33A:609–620

7. Henderson JB, Wiebelt JA, Tant MR (1985) A model for the thermal response of polymer composites materials with experimental verification. J Compos Mater 19:579–595
8. Gibson AG, Wu YS, Chandler HW, Wilcox JAD, Bettess P (1995) A model for the thermal performance of thick composite laminates in hydrocarbon fires. Revue de l'Institute Francais du Petrole 50:69–74
9. Looyeh MRE, Bettess P, Gibson AG (1997) A one-dimensional finite element simulation for the fire-performance of GRP panels for offshore structures. Int J Numer Methods Heat Fluid Flow 7:609–625
10. Gibson AG, Wright PNH, Wu YS, Mouritz AP, Mathys Z (2003) Modelling residual mechanical properties of polymer composites after fire. Plast Rubbers Compos: Process Appl 32:81–90
11. Mouritz AP, Mathys Z (2001) Post-fire mechanical properties of glass-reinforced polyester composites. Compos Sci Technol 61:475–490
12. Kulkarni AP, Gibson RF (2003) Nondestructive characterization of effects of temperature and moisture on elastic moduli of vinyl ester eesin and E-glass/vinyl ester composite. In: Proceedings of the American Society of Composites 18th annual technical conference. Florida
13. Huang H, Kardomateas GA (2002) Buckling and initial postbuckling behavior of sandwich beams including transverse shear. AIAA J 40:2331–2335
14. Gibson AG, Mouritz AP, Mathys Z (2004) The integrity of polymer composites during and after fire. J Compos Mater 38:1283–1306
15. Liu L, Holmes JW (2007) Experimental investigation of the buckling of polymeric composites during high simultaneous heat flux exposure and compressive loading. J Compos Mater 41(2):211–241
16. Liu L (2006) Durability of polymer composite materials, PhD Thesis, School of Aerospace Engineering, Georgia Institute of Technology, Atlanta, GA
17. Liu L, Kardomateas GA, Birman V, Holmes JW, Simitses GJ (2006) Thermal bending of a heat exposed, axially restrained composite column. Compos Part A 37(7):972–980. (Special Issue on Fire Behaviour of Composites)
18. Bausano JV, Boyd SE, Lesko JJ, Case SW (2004) Composite life under sustained compression and one sided simulated fire exposure: characterization and prediction. In: Composites 2004 convention and trade show American Composites Manufacturers Association. Tampa, FL